Generation and Reconstruction of OAM Light States Using Spatial Light Modulators

Jeremy Ronald Binda

Bachelorarbeit in Physik
angefertigt im Institut für Angewandte Physik

vorgelegt der
Mathematisch-Naturwissenschaftlichen Fakultät
der
Rheinischen Friedrich-Wilhelms-Universität
Bonn

Februar 2024

Ich versichere, dass ich diese Arbeit selbstständig verfasst und keine anderen als die angegebenen Quellen und Hilfsmittel benutzt sowie die Zitate kenntlich gemacht habe.

Bonn, 04.02.2025 ..... Jenny Binda .....

Datum Unterschrift

1. Gutachter: Prof. Dr. Sebastian Hofferberth
2. Gutachter: Jun. Prof. Dr. Daqing Wang

Contents

CHAPTER 1

Introduction

In recent decades, the orbital angular momentum (OAM) of light has garnered interest in various fields, both in its generation and measurement [1–5] and applications in quantum cryptography, as OAM conservation allows for quantum information transfer [6–9]. The field of atomic physics likewise holds an interest in OAM light for optical tweezer arrays [10, 11] and OAM atom-photon interactions [12], the latter being the greater purpose of this thesis.

The Rubidium Quantum Optics (RQO) experiment at the University of Bonn's Institute of Applied Physics aims to realize a quantum nonlinear medium for single photons by using highly excited Rydberg atoms to mediate strong photon interactions. This process relies on the strong interactions of ultracold ensembles of Rydberg atoms which are mapped onto otherwise non-interacting single photons via electromagnetically-induced transparency [13]. Such quantum nonlinearities hold significant application in quantum computing, in addition to their fundamental interest. In the experiment, Rb atoms are first laser-cooled in a magneto-optical trap (MOT) before being transfered into a large dipole trap where the atomic cloud is cooled to approximately 4 μK. It is here where the atoms are probed with few-photon pulses and the nonlinear Rydberg-mediated interactions realized.

Up until now in the experiment, the Rb atoms have been probed with few-photon pulses of a Gaussian TEM_{00} laser, and the outgoing light collected in a single mode fiber (SMF) after the photons pass through the Rb cloud and experience Rydberg-mediated interactions. This method neither allows for radial/OAM control of the probe beam before, nor radial/OAM measurement after the Rb cloud. In this way, any information about the effect of Rydberg-mediated photon interactions on these properties of the light is lost, as well as the experimental freedom to probe the cloud of Rydberg atoms with varying OAM and/or radial distributions of light.

This thesis is the third iteration of the ongoing SLM project within the RQO group that looks to implement a spatial mode filtering system into the main experiment. Compared to its predecessors, this thesis focuses more on the reconstruction of OAM states using a dual SLM apparatus, and mostly picks up from where previous bachelor's students left off rather than attempting to re-establish the previous results. Kimberly's thesis [14], for instance, establishes the fundamental laser, Fourier optical, and SLM operational theory of the topic, while Celina's thesis [15] focuses on simulation and analysis of the experimental results, the codes from which forming the basis for many of mine. Both were excellent resources that I have continuously referenced in my work, and are worth the attention of the reader, as I have intentionally abbreviated and omitted many topics that have already been rigorously covered by them in order to avoid repetition.

This thesis is divided into three main chapters of content; the first chapter re-addresses many topics which, although they may have already been covered in previous theses, are fundamental theoretical concepts for the entire work. The second chapter continues from the previous Bachelor project: using a single SLM setup to generate pure Laguerre-Gauss (LG) modes and analyzing them for theoretical accuracy, etc.; extending this analysis to superpositions of LG modes; and introducing the 4f system in order to incorporate the second SLM. The second half of the second chapter then sees the introduction of the second SLM into the setup and catalogues the first projective measurements. In the third chapter we introduce an SMF into the setup that is used to measure the mode coincidence matrices of different radial mode regimes. Here several measurements are done to analyze and optimize these relations and finally reconstruct a state of superimposed LG modes. This leaves the project in a state not too far from its ultimate implemenation into the main experiment, which should be possible once the shortcomings discussed in the Outlook 5 have been addressed.

CHAPTER 2

Laguerre-Gauss Modes and their Generation

In this chapter we cover all of the theoretical considerations for the generation of LG modes in the experiment. In sec. 2.1 we start by mathematically defininining LG modes and analyzing some of their relevant properties. Next, in sec. 2.2 we turn to spatial light modulators (SLM's) as the chosen device that is capable of generating these modes, and describe the method of implementing this device in order to generate LG modes. Lastly, in sec. 2.3 we analyze the Fourier optics that are required to observe the generated LG modes, which forms the basis of many of our experimental considerations, and also mathematically describes our experiment.

2.1 The Set of Laguerre-Gauss Modes

In the experiment, we look to exhibit OAM and radial control over the laser by converting the incoming Gaussian beam into LG modes, which characteristically possess both these attributes. This set of modes is orthonormal and complete, which we later see allows us to uniquely decompose any beam into its constituent modes. This is a characteristic that is a necessity for later efforts of reconstructing these modes. We now describe these modes and their superpositions, and analyze their resulting properties.

2.1.1 The Paraxial Helmholtz Equation

Within the frame of this thesis we are interested in monochromatic and paraxial[1] scalar electric fields where the transverse scalar electric field (or mode) remains both time-independent and has a slowly varying envelope along the axis of propagation z. We omit a full derivation of the paraxial Helmholtz equation of eq. 2.1 for brevity, however a detailed derivation using the aforementioned characteristics to approximate the wave equation can be found in the German-language script of Prof. Linden's *physik311* lecture p. 3-10, 24 [16] or Goodman p. 36 [17]. The paraxial Helhmoltz equation describes the mode of an electromagnetic wave and reads

$$\nabla_{\perp}^{2} A - i2k \frac{\partial A}{\partial z} = 0 \tag{2.1}$$

[1] near-axis, where the transverse mode doesn't extend far beyond the optical axis

with $\nabla_\perp^2 = \partial_x^2 + \partial_y^2$, the real scalar amplitude of the electric field A, and the wave number $k = \frac{2\pi}{\lambda}$. We can combine the amplitude A with the phase Φ to define the scalar electric field

$$u(\vec{r}) = A(\vec{r})e^{i\Phi(\vec{r})} \tag{2.2}$$

From eq. 2.2 we can see that the amplitude $A(\vec{r})$, phase $\Phi(\vec{r})$, and intensity $I(\vec{r})$ of an arbitrary field $u(\vec{r})$ can be easily calculated using eq. 2.3–2.5.

$$\Phi(\vec{r}) = \arg(u(\vec{r})) \tag{2.3}$$
$$A(\vec{r}) = |u(\vec{r})| \tag{2.4}$$
$$I(\vec{r}) \propto |u(\vec{r})|^2 \tag{2.5}$$

2.1.2 Laguerre-Gauss (LG) Modes

The Laguerre-Gauss modes are a complete and orthonormal family of solutions to eq. 2.1 in cylindrical coordinates. The scalar field of a Laguerre-Gauss mode with the radial mode index $p \in \mathbf{N}$ and the orbital angular momentum $l\hbar$, $\ell \in \mathbf{Z}$ that is focussed at $z = 0$ is defined as [3]

$$\begin{aligned}\mathrm{LG}_{p,\ell}(r,\phi,z) =& (-1)^p \left[\frac{2}{\pi}\frac{p!}{(p+|\ell|)!}\right]^{1/2} \frac{(\sqrt{2}\xi)^{|\ell|}}{w_z} \exp(-\xi^2) L_p^{|\ell|}(2\xi^2) \exp(-i\ell\phi) \\ &\times \exp(-i\xi^2 z/z_R) \exp(i(2p+|\ell|+1)) \arctan(z/z_R)\end{aligned} \tag{2.6}$$

with the set of generalized Laguerre polynomials $L_p^{(\ell)}(x)$ given by the Rodrigues formula,

$$L_p^{(\ell)}(x) = \frac{x^{-\ell}e^x}{p!}\frac{\mathrm{d}^p}{\mathrm{d}x^p}\left(x^{\ell+p}e^{-x}\right) \tag{2.7}$$

the Rayleigh length of the laser z_R, and the waist of the laser w_z at a propagation distance z. Here we have also abbreviated $\xi := r/w_z$. The variable l is sometimes called the topological charge of the beam as it defines the helical structure of its phase. As a shorthand we introduce the Bra-Ket notation. Although we are only dealing with classical light, the completness and orthormality of the LG eigenfunctions leads to a similar mathematical structure as in quantum mechanics, which we emphasize with this notation

$$|p,\ \ell\rangle := \mathrm{LG}_{p,\ell} \tag{2.8}$$

As such a pseudo-quantum state, we must define the inner product of two LG modes $\mathrm{LG}_{p,\ell}$ and $\mathrm{LG}_{p',\ell'}$

$$\langle p',\ \ell'|p,\ \ell\rangle := \int_0^\infty \int_0^{2\pi} \mathrm{LG}^*_{p',\ell'}\,\mathrm{LG}_{p,\ell}\,\mathrm{d}r\mathrm{d}\phi \tag{2.9}$$

By applying the orthonormality of the LG modes, we can simplify eq. 2.9 to the important relation

$$\langle p',\ \ell'|p,\ \ell\rangle = \delta_{p',p}\delta_{\ell',\ell} \tag{2.10}$$

2.1.3 Properties of Laguerre-Gauss Modes

As a property of the completeness of the set of Laguerre-Gauss Modes $\{|p,\ \ell\rangle\}$, it spans the solution space of the paraxial Helmholtz equation, such that any solution u of eq. 2.1 can be expressed as a superposition of LG eigenstates with complex superposition coefficients $\alpha_{p,\ell}$ and a real normalizing factor N such that $\langle u|u\rangle = 1$ [2]

$$u(\vec{r}) = \frac{1}{N}\sum_{p,\ell}\alpha_{p,\ell}\,|p,\ \ell\rangle \tag{2.11}$$

Equivalently, one can write

$$\sum_{p,\ell}|\langle p,\ \ell|u\rangle|^2 = 1 \tag{2.12}$$

such that any arbitrary solution of the paraxial Helmholtz equation u has a unique LG mode decomposition[3]. Using eq. 2.3–2.5 one can calculate the amplitude A, phase Φ, and intensity pattern I of any pure LG eigenstate or superposition of LG eigenstates of eq. 2.11.

Similarly, we can express the phase $\gamma_{p,\ell} \in \mathbb{R}$ and amplitude $\beta_{p,\ell} \in \mathbb{R}$ of the complex superposition coefficients $\alpha_{p,\ell}$ by calculating their argument and absolute value

$$\alpha_{p,\ell} = |\alpha_{p,\ell}|e^{i\arg(\alpha_{p,\ell})} \tag{2.13}$$

$$=: \beta_{p,\ell}e^{i\gamma_{p,\ell}} \tag{2.14}$$

We visualize eq. 2.11 and 2.14 in fig. A.1 by respectively superimposing an unscaled ($\alpha = 1$), a phase-delayed($\gamma \neq 0$), and a weighted ($\beta \neq 0$) LG_{20} mode onto an LG_{22} mode and calculating the amplitude, phase, and intensity. Each quantitity is scaled by normalizing with its respective maximum value, such that it only assumes values between 0 and 1. The $\beta_{p,\ell}$ are of special interest in later sections, as eq. 2.15 describes a mode projection measurement which allows the later reconstruction of LG superpositon states based on their LG mode decomposition.

$$|\langle p,\ \ell|u\rangle|^2 = |\alpha_{p,\ell}|^2 = \beta_{p,\ell}^2 \tag{2.15}$$

2.2 Spatial Light Modulators (SLM's) and their Operation

We choose SLM's as our means of generating LG modes due to their relative ease-of-use, commercial availability, and high levels of accuracy (as is later experimentally confirmed). We now look to understand their operation as it is relevant to their implementation in the experiment. This includes the further step of understanding how they can can be properly implemented to generate LG modes, and how these modes can thus be observed.

[2] One can set $N = 1$ by otherwise requiring that the sum of the absolute squares of the superposition coefficients is equal to unity.

[3] Only the electric field, not its corresponding intensity, possesses this uniqueness as a consequence of eq. 2.15

2.2.1 Operational Principles of an LCOS-SLM

A spatial light modulator is essentially a pixelated waveplate, in that it retards incoming light differently depending on its spatial position and its polarization. We implement two SLM's in this experiment for the generation and the reconstruction of LG modes. Both SLM's are LCOS[4]-SLM's: the Hamamatsu X13267-02 and the Santec SLM-100. A summary of the most relevant specifications taken from their respective data sheets [18]–[19] is listed in tab. 2.1

Spec	Hamamatsu	Santec
SLM bit	8	10
square pixel width ($x \times y$)	792×600	1440×1050
pixel pitch	12.5 µm	10.4 µm
LCOS axis	x	x

Table 2.1: Summary of Hamamatsu and Santec SLM specifications

Physically speaking, an LCOS-SLM is an array of birefringent voltage-steered liquid crystal pixels in which each respective pixel can be individually steered to have a certain retardance between $[0, 2\pi]$ for the linear polarization component in the LCOS-axis of light of a given wavelength. The LCOS axis of each SLM is the x- or horizontal axis, and only the electrical field component in this axis experiences any modulation from the SLM. In order that the incoming light be maximally modulated, in the experiment the incoming beam is always horizontally polarized in the x-axis (with the sole exception of sec. 4.2.3).

Fig. 2.1 is an illustration of the cross section of five adjacent pixels. As an incoming beam is first modulated then diffracted by the SLM, certain spatial regions of it experience certain phase delays, and, when additionally displaying a grating pattern on the SLM as we do in the experiment, other regions can effectively be removed by diffracting them into a different order via the same process, which allows for both phase and amplitude control of the incoming light. In the experiment we only observe the first order of diffraction, as is covered in more detail in the next section.

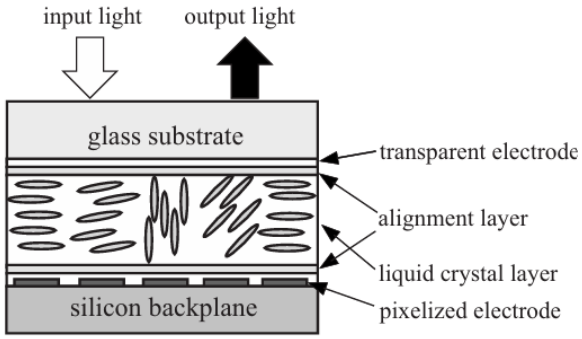

Figure 2.1: Technical structure of an LCOS SLM, taken from [5]

We manually control the SLM's via the respective graphical user interfaces (GUI's) from the manufacturers and a Windows PC connection. The PC recognizes the SLM as a monitor via a DVI

[4] liquid crystal on silicon

cable connection and displays a live image on it. The voltage information for each pixel is contained in this image, which we call a phase mask or computer generated hologram (CGH). The phase masks contain the same pixel dimensions as the SLM screen and are in n-bit grayscale, corresponding to the bit count of the SLM pixels; assuming an ideal calibration, black or 0 bits corresponds to a $\Psi = 0$ phase shift while white or $2^n - 1$ bits corresponds to a $\Psi = 2\pi$ in a strictly linear relation.

As the SLM's operation relies on the birefringence of the liquid crystals, their steering voltages must be calibrated such that the their phase retardance stays within the bounds $\Psi \in [0, 2\pi]$ for the wavelength of the laser. For this reason, each SLM has a wavelength setting in their GUI that we constantly leave at the wavelength of our laser 780 nm.

2.2.2 Calculating Computer-Generated Holograms (CGH's) for an SLM

By calculating a specific hologram we give the SLM the sufficient information to diffract the desired output electric field into the first diffraction order that we are observing. For the generation of holograms we follow the paper by Bolduc, et. al. [6]. Starting from a desired output field $E(m, n)$ and assuming an incoming homogenous plane wave, we first calculate the phase $\Phi(m, n)$ and amplitude $A(m, n)$ via eq. 2.3–2.4 in the discrete pixel coordinates of the SLM $\{m, n\}$ with m being the LCOS axis. We then calculate the analytical function $0 \leq \mathcal{M} \leq 1$ related to the amplitude modulation and $\mathcal{F}$ which relates the amplitude to the phase

$$\mathcal{M}(m, n) = 1 + \frac{1}{\pi}\text{arcsinc}(A(m, n)) \tag{2.16}$$

$$\mathcal{F}(m, n) = \Phi(m, n) - \pi\mathcal{M} \tag{2.17}$$

We now combine $\mathcal{M}$ and $\mathcal{F}$ with a blazed[5] grating $\mathcal{G}(m) = \frac{2\pi m}{\Lambda}$ of the grating period Λ. This serves to diffract the difference between the incoming field and the desired first-order outgoing field into higher orders such that they do not interfere with first order. We then get the final expression for the phase information of the hologram $\Psi(m, n)$

$$\Psi(m, n) = \mathcal{M}\,\text{Mod}\,(\mathcal{F} + \mathcal{G},\, 2\pi) \tag{2.18}$$

In order to motivate this choice of phase profile $\Psi(m, n)$, we now analyze the resulting field in the first order of diffraction. After passing through a hologram with the phase profile of eq. 2.18, the incoming plane acquires the form $T(m, n)$

$$T(m, n) = e^{i\mathcal{M}\,\text{Mod}(\mathcal{F}+\mathcal{G},\,2\pi)} \tag{2.19}$$

A further calculation based on a Fourier-Taylor expansion yields the Fourier transform of the electric field of the first order of diffraction

$$T_1(m, n) = -\text{sinc}(\pi\mathcal{M} - \pi)e^{i(\mathcal{F}+\pi\mathcal{M})} \tag{2.20}$$

Substituting eq. 2.16–2.17 into eq. 2.20 one recovers the desired output field $T_1 = -Ae^{i\Phi}$ in the Fourier spectrum of the first order with an irrelevant phase delay of π. This solution is in fact

[5] a grating that predominantly diffracts into the first order in order to maximize diffraction efficiency

exact, although computationally quite expensive since the arcsinc function must be calculated via relaxation method, as a suitable function does not exist in Scipy. There are computationally lighter approximations which we don't use in this thesis, but were thoroughly analyzed in the previous Bachelor project [15]. For generation of LG modes[6], one need only define the desired output field according to eq. 2.11 and follow this procedure.

2.3 Fourier Optics Description

Given our definition of $\Psi(m,n)$ in eq. 2.18 for the generation of phase masks, we now look to observe the Fourier spectrum of the first order of diffraction from the SLM, as this will be our desired output field. Before turning our attention to the further experimental considerations that allow an observation of this Fourier spectrum, we first seek to derive an expression for the field at the screen of the SLM. For an SLM of $N_x \times N_y$ pixels of the dimensions $d_x \times d_x$ displaying the phase mask $\Psi(m,n)$ with the discrete pixel coordinates $\{m,n\}$, the total output field at the screen $u_{\mathrm{SLM}}(x,y)$ is given by [20] [7]

$$u_{\mathrm{SLM}}(x,y) = \sum_{m=0}^{N_x-1}\sum_{n=0}^{N_y-1} e^{i\Psi(m,n)}\,\mathrm{rect}\left(\frac{x}{d_x} - m - \frac{N_x}{2}\right)\cdot \mathrm{rect}\left(\frac{y}{d_y} - n - \frac{N_y}{2}\right) \tag{2.21}$$

with the $\mathrm{rect}(x)$ function

$$\mathrm{rect}(x) = \begin{cases} 1 & : -1/2 \le x \le 1/2 \\ 1/2 & : |x| = 1/2 \\ 0 & : \text{otherwise} \end{cases} \tag{2.22}$$

After being modulated by the SLM, the light is then diffracted by the SLM screen. The Fresnel diffraction integral of equation 2.23 describes the electric field $u(x,y)$ of light of the wavelength λ at a propagation distance z after passing through an aperture $\{\xi,\eta\}$ at which the incident electric field at the aperture $u(\xi,\eta)$ is known . This describes the propagation of the modulated field after it is diffracted by the SLM and propagates for some distance. For a complete derivation, see Goodman chap. 3–4 [17]

$$u(x,y) = \frac{e^{ikz}}{i\lambda z} e^{i\frac{k}{2z}(x^2+y^2)} \int_{-\infty}^{\infty}\int_{-\infty}^{\infty} u(\xi,\eta) e^{i\frac{k}{2z}(\xi^2+\eta^2)} e^{-i\frac{k}{z}(x\xi+y\eta)} \mathrm{d}\xi\mathrm{d}\eta \tag{2.23}$$

The Fresnel diffraction integral is a near-field approximation of the Huygens-Fresnel diffraction integral. It is valid for sufficiently small propagation distances z that do not fulfill eq. 2.24, which is known as the Fraunhofer condition. Calculating the necessary z for our wavelength $\lambda = 780\,\mathrm{nm}$ and the SLM screen $\{\xi,\eta\}$ such that the Fresnel approximation be invalid would show this distance to be far too large to be experimentally plausible. We are thus well within the boundaries for this approximation

[6] As one can see in eq. 2.18 the phase mask calculation process is highly nonlinear, such that the hologram of an LG mode superposition is expressly not equal to the sum of the holograms of the respective modes.

[7] The difference between eq. 2.19 and eq. 2.21 arises from a consideration of the finite extent of the SLM pixels and screen.

$$z >> \frac{k(\xi^2 + \eta^2)}{2} \tag{2.24}$$

We now assume that the electric field is diffracted by the SLM into its near field, and propagates a distance d until a lens; the reasoning behind this will be revealed later. We describe this as a translation in the Fourier spectrum of the diffracted field $\mathcal{F}[u_{\text{SLM}}](f_x, f_y)$ using the Fresnel approximation of eq. 2.23 and the Fourier transform shift property $\mathcal{F}[f(\xi - a)](x) = e^{-2\pi i a x}\mathcal{F}[f(\xi)](x)$. This results in the Fourier spectrum $\mathcal{F}[u_{\text{lens}}](f_x, f_y)$ before the lens, in the frequency domain coordinates $f_{x/y} := \frac{x/y}{\lambda f}$. We hereby neglect an irrelevant constant phase term, see Goodman p. 101–106 [17]

$$\mathcal{F}[u_{\text{lens}}](f_x, f_y) = e^{-i\pi\lambda d(f_x^2 + f_y^2)}\mathcal{F}[u_{\text{SLM}}](f_x, f_y) \tag{2.25}$$

After the input field u_{lens} then passes through a lens of the focal length f, its output field in the focal plane of the lens is given by u'_{lens}

$$u'_{\text{lens}}(x, y) = e^{-i\frac{k}{2f}(x^2+y^2)}u_{\text{lens}}(x, y) \tag{2.26}$$

If we now substitute eq. 2.25 into eq. 2.26, we calculate the final output field $u_f(x, y)$ in the focal plane of the lens

$$u_f(x, y) = \frac{e^{\frac{ik}{2f}(1-\frac{d}{f})(x^2+y^2)}}{i\lambda f}\mathcal{F}[u_{\text{SLM}}](f_x, f_y) \tag{2.27}$$

$$= \frac{e^{\frac{ik}{2f}(1-\frac{d}{f})(x^2+y^2)}}{i\lambda f}\int_{-\infty}^{\infty}\int_{-\infty}^{\infty} u_{\text{SLM}}(\xi, \eta)e^{-i\frac{2\pi}{\lambda f}(x\xi+y\eta)}\mathrm{d}\xi\mathrm{d}\eta \tag{2.28}$$

Eq. 2.28 thus describes the final field after the inital field at the SLM screen u_{SLM} propagates a distance d to a lens of focal length f and is then observed in the focal plane of the lens. By design, this equation is exactly the output field where we can observe our desired output field in the first order of diffraction, as it is the Fourier transform of the field at the SLM screen plus a phase term. For a single SLM setup the additional variable radial phase factor is irrelevant, as it cancels out when squaring. However, with a second SLM it is not negligible, such that we must neutralize it by later requiring $d = f$, as we do when we implement the 4f system in sec. 3.1.3. This calculation is an example of the Fourier-transforming property of a lens, which we have applied in eq. 2.26 to Fourier transform the propagated field from the screen of the SLM.

To further understand eq. 2.28, we now calculate the the Fresnel approximation of eq. 2.23 in the case of the Fraunhofer condition being fulfilled. This allows us to neglect the quadratic aperture coordinates ξ^2, η^2 against a large z. Doing so yields the so-called Fraunhofer diffraction integral, the far-field approximation for the diffracted incident light u.

$$u_f(x, y) = \frac{e^{ikz}}{i\lambda z}e^{i\frac{k}{2z}(x^2+y^2)}\int_{-\infty}^{\infty}\int_{-\infty}^{\infty} u(\xi, \eta)e^{-i\frac{k}{z}(x\xi+y\eta)}\mathrm{d}\xi\mathrm{d}\eta \tag{2.29}$$

Comparing eq. 2.29 with eq. 2.28 we notice an equality except for the phase terms. We can thus see that by implementing the lens to Fourier transform the diffracted near field, we have effectively Fourier transformed the near field into its far field, thus bypassing the experimental difficulty of fulfilling eq.

2.24 and Fourier transforming solely via propagation.

CHAPTER 3

Experimental Implementation of the SLM's

Now that we have established its theoretical foundations, we turn to the experiment where we can begin to generate LG modes. In sec. 3.1 we start with a single SLM, first in a setup with a telephoto lens with which we generate and image various LG modes and analyze their quality. Next we switch to a 4f system, which can accomodate a second SLM, and image a selection of superimposed modes using this setup. In sec. 3.2 we then incorporate the second SLM into the 4f system and, using a beam profiler, image the results of mode projection measurements between the two SLM's.

3.1 Single SLM System

The ultimate goal of this thesis is to realize a similar system as Bolduc, et al. [6] as a mode sorting system. Before being able to measure these mode coincidence matrices of chap. 4, we must first investigate the (analytical) purity of the generated LG modes, in order to ensure that our generation methods are sufficiently precise.

3.1.1 Experimental Setup

We first implement the setup of fig. 3.1 to analytically investigate the quality of the generated LG modes from SLM A. This setup was originally built by Kimberly and later adjusted by Celina, however we did a full realignment of the optics. More detailed considerations for this setup can be found in Kimberly's thesis [14].

The section before the first SLM serves to create a maximally modally pure and x-polarized Gaussian beam to be diffracted by the first SLM. It consists first of a 780 nm laser [21] and an optical isolator to prevent back reflections from damaging the laser. The beam then continues through some mirrors and (optionally) some OD filters to a half waveplate that changes its polarisation axis to align with that of a polarization-maintaining single mode fiber (SMF), into which the beam then couples, thus "cleaning" out non-Gaussian components. After outcoupling the beam passes through a telescope ($f_1 = 30$ mm planoconvex, $f_2 = 100$ mm planoconvex) which firstly serves to collimate the beam, and secondly expands the beam radius such that it covers a larger area of the SLM screen and thus experiences a higher resolution. Lastly, it passes through another half waveplate to match the polarization axis of the beam to the LCOS axis of the SLM, before it is then diffracted from the first SLM. Here it is crucial that the angle of incidence remain less than 5° in order to avoid a large distortion from the true pixel

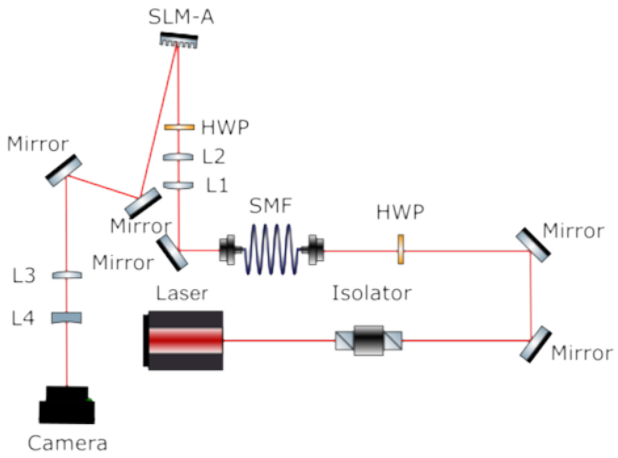

Figure 3.1: Setup for single SLM measurements

shape. The first order is then selected via an iris, and reflected along mirrors until it passes through a telephoto lens ($f_3 = 150\,\text{mm}$ planoconvex, $f_4 = -100\,\text{mm}$ planoconcave) that Fourier transforms the beam into its far field and reduces the radius to a reasonable size for the camera. At the focal plane of the telephoto lens a beam profiler is placed in order to capture the intensity pattern.

3.1.2 Generation and Analysis of LG Pure Mode States

We now use the setup of fig. 3.1 to image and analyze the purity of the LG modes which we generate with SLM A. The images in the left of fig. 3.2 were taken with a beam profiling camera[1] that has a resolution of 1280×1024 pixels and a square pixel width of $6.5\,\mu\text{m}$ [22]. For illustrative purposes the holograms used are also shown to the right. The y-axis is the topological charge ℓ and the x-axis is the radial mode index p, starting from LG_{00} in the top-left corner. For the measurement we use phase masks calculated for a waist of $w_0 = 30$ SLM A pixels.

Without a second SLM, we have no mode decomposition method of analyzing the purity of these generated modes. For this reason, we instead analyze them analytically by calculating the R^2 values of the observed modes with their theoretical expectations of eq. 2.6. The coefficient of determination, or R^2 value of a functional fit f_i of the data points y_i and their mean $\bar{y}$ is given by eq. 3.1. It is a measure of the suitability of the fit of the data points and only assumes values between 0 (lower asymptotic limit) and 1 (perfect).

$$R^2 = 1 - \frac{\sum(y_i - f_i)^2}{\sum(y_i - \bar{y})^2} \tag{3.1}$$

We read the data from the images in fig. 3.2, use the camera specifications to convert the image into physical spatial units, perform a fit, and visualize the resulting R^2 values in fig. 3.3.

These values are a slight improvement from previous results from Celina [15] p. 39, in that the R^2 are univerally a bit higher, and thus more closely match her theoretical calculations of p. 24. We also

[1] LaserCam-HR II by Coherent Laser Technologies

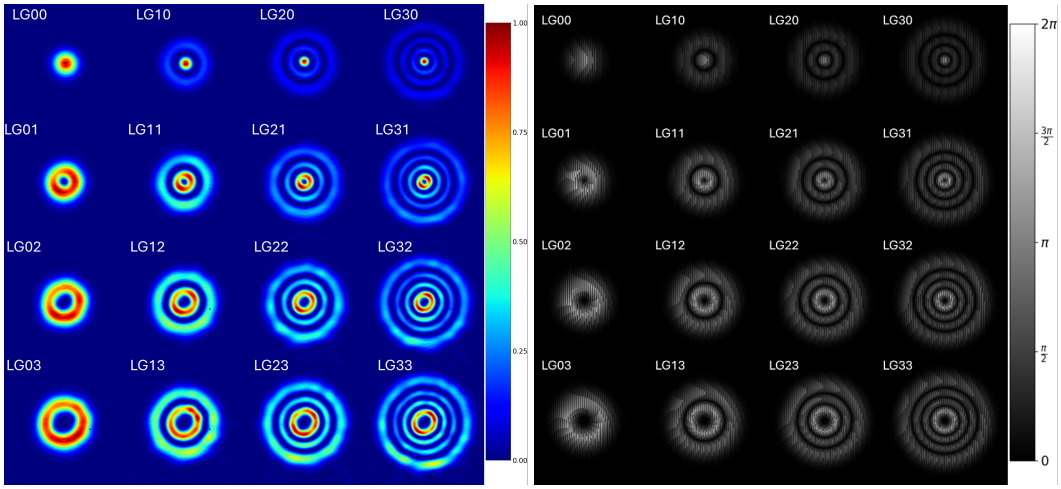

Figure 3.2: Composite image of LG_{00}–LG_{33} generated with a single SLM and its phase masks

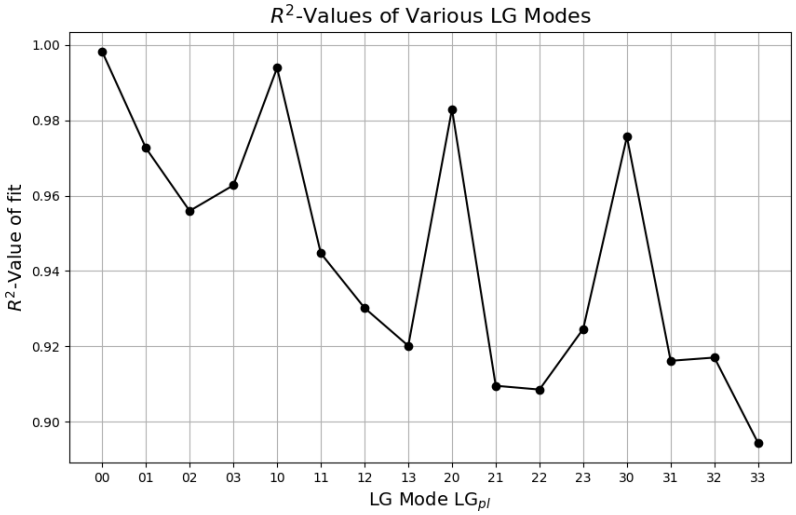

Figure 3.3: R^2 values of various LG modes using single SLM setup

can observe the trend of the coefficient of determination decreasing for higher topological charges ℓ. The results are quite comparable to those of Matsumoto fig. 18 [5], who for instance measure an R^2 of around 0.9 for LG_{33}, and also observe a similar trend for the topological charges. Following these results, this would suggest a theoretical mode purity of approximately $0.70 - 0.85$ for the various modes, as was theoretically calculated in the same paper.

3.1.3 Imaging in a 4f system

The two SLMs are to be placed in a 4f system, which consists of two lenses of equal focal lengths f and one iris all placed equidistantly from each and the two SLM's at distances of f, with the iris between the two lenses. The reasoning behind this choice of setup is that, through it, the electric field at the screen of the first SLM is imaged 1:1 to the screen of the second SLM without any additional phase factors. More detailed considerations about this choice of configuration as well an alternative 2f system are discussed in [4]. Starting with eq. 2.28, we first calculate the field u_f in the focal plane of the first lens after the field at the first SLM u_{SLM} has propagated a distance $d = f$ to the lens and passed through it. This is exactly equivalent to the Fourier transform of u_{SLM}

$$u_f(x,y) = \int_{-\infty}^{\infty}\int_{-\infty}^{\infty} u_{\text{SLM}}(\xi,\eta)e^{-i\frac{2\pi}{\lambda f}(x\xi+y\eta)}\mathrm{d}\xi\mathrm{d}\eta \tag{3.2}$$

The resulting field, in the focal plane of the first lens which is also the aperture of the iris, now propagates another distance $d = f$ to the second lens, through which it then passes, thus similarly Fourier transforming it at it the focal plane of the lens. This field is likewise equal to the Fourier transform of u_f, also without an additional phase term since $d = f$

$$u(u,v) = \int_{-\infty}^{\infty}\int_{-\infty}^{\infty} u_f(x,y)e^{-i\frac{2\pi}{\lambda f}(ux+vy)}\mathrm{d}x\mathrm{d}y \tag{3.3}$$

Substituting eq. 3.2 into eq. 3.3 we see that the field at the focal plane of the second lens, which is where we place the second SLM, is the same as the field at the screen of the first SLM, with unit magnification and an inverted image (which is irrelevant for us due to the rotational symmetry of the LG modes)

$$u(u,v) = \int_{-\infty}^{\infty}\int_{-\infty}^{\infty}\int_{-\infty}^{\infty}\int_{-\infty}^{\infty} u_{\text{SLM}}(\xi,\eta)e^{-i\frac{2\pi}{\lambda f}(x\xi+y\eta)}\mathrm{d}\xi\mathrm{d}\eta e^{-i\frac{2\pi}{\lambda f}(ux+vy)}\mathrm{d}x\mathrm{d}y \tag{3.4}$$

$$= u_{\text{SLM}}(-\xi,-\eta) \tag{3.5}$$

The plane of the iris aperture which is also the focal plane of the first lens is aptly called the Fourier plane. The iris is quite meaningful to place here, as its finite extent filters out k-vector components from the other orders of diffraction in order to reduce disturbances to the desired output mode in the first order.

We now implement this 4f system using two 500 mm lenses after the first SLM. Before we incorporate the second SLM, we check the quality of the alignments by placing the beam profiler in the plane of the second SLM and taking some images. The complete setup is pictured in fig. 3.4.

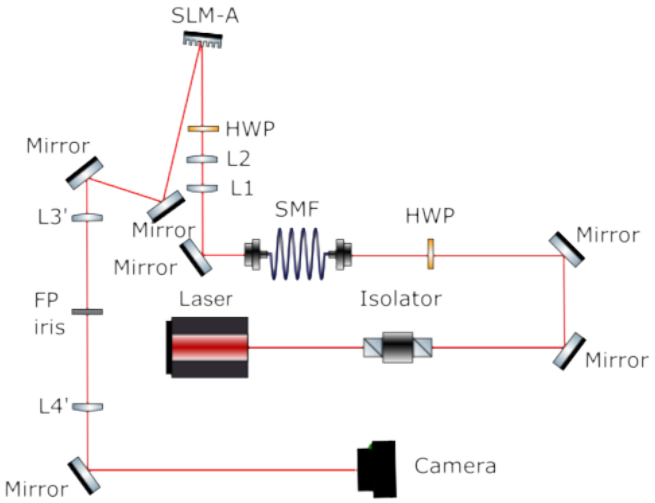

Figure 3.4: 4f system for a single SLM with a camera positioned in the final focal plane

3.1.4 Generation of LG Mode Superposition States

Here we test the 4f system after the first SLM by experimentally generating some superimposed LG modes (left) and qualitatively comparing them with the mathematical expectation (right) in fig. 3.5. [2] Of particular interest are the flower patterns of the form $\mathrm{LG}_{0n} + e^{i\gamma}\mathrm{LG}_{0-n}$, but in essence the modes we choose are completely arbitrary. We image and calculate the mathematical expectation for the modes:

$$
\begin{aligned}
E_1(w_0 = 50) &= \mathrm{LG}_{0,4} + e^{-i\frac{\pi}{2}}\mathrm{LG}_{0,-4} \quad \text{(top left)} \\
E_2(w_0 = 30) &= \mathrm{LG}_{0,5} + e^{-i\pi}\mathrm{LG}_{0,-5} \quad \text{(top right)} \\
E_3(w_0 = 30) &= \mathrm{LG}_{1,2} + e^{-i\frac{\pi}{2}}\mathrm{LG}_{1,-2} \quad \text{(bottom left)} \\
E_4(w_0 = 80) &= \mathrm{LG}_{2,2} \quad \text{(bottom right)}
\end{aligned}
$$

There is a lot of unexplored potential in these superpositions that could be further investigated. For instance, we already see that E_3 could not quite be fully resolved; is this a consequence of each respective constituent mode or merely the superposition we chose? As can be seen in fig. 3.3, higher topological charges of a pure mode generally lead to a lower analytical mode purity; does this also apply for superpositions, and how does changing the topological charge of one constituent mode affect the whole? Either way, we qualitatively observe a very high similarity of the experimental images to the mathematical expectation, and confirm the efficacy of our 4f system.

[2] In principle, this could also have been done with the setup from fig. 3.1, but the mode superposition phase masks weren't ready until after the setup had already been changed.

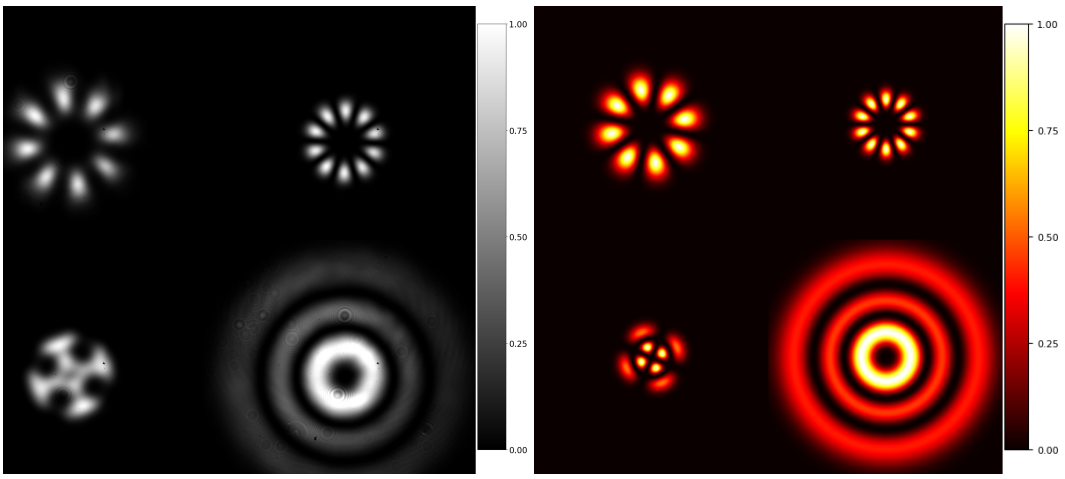

Figure 3.5: Composite image of experimental superimposed modes (left) and mathematical expectations (right)

3.2 Dual SLM System

One may see fig. 3.2 and 3.3 and ask themself why we need a second SLM in the first place if we can already image and analytically investigate the purity of the generated modes. Other than this measuring process being quite inconvenient and the measure of mode purity being analytical and not quantum mechanical, the simple answer is that the images are informationally incomplete. A simple analogy is a polarisor and analysor. The polarisor (first SLM) creates a specific polarization state of the light while the analysor (second SLM) projects a different state onto it. By projecting various polarization states onto the original state and measuring the power, one can deduce the polarization state from the first polarisor. Without an analysor one would have no information about the polarization state, besides the simple observable fact that it's power has decreased by $\frac{1}{2}$.

Likewise, with a single SLM we can take the absolute square of eq. 2.28 and measure the output intensity from the first SLM, however in doing so we lose all information about the phase. If we were to for instance conjugate the output field ($Ae^{i\Phi} \mapsto Ae^{-i\Phi}$) of a state from SLM A, we would observe the same intensity pattern as before, despite the field having a completely different phase. Now if we generate a state $|p, \ell\rangle$ on SLM A and project the mode $\langle p, \ell|$ onto it with SLM B, eq. 2.10 becomes unity and we revert the state back to the state before SLM A, the Gaussian mode[3]. On the other hand, if we conjugate the state generated by SLM A, eq. 2.10 is no longer unity and the Gaussian beam is no longer restored, as some component of eq. 2.21 from the first SLM has not been modulated back to Gaussian. In this manor, we can implement the second SLM as a mode filtering device; by projecting LG modes onto the modes generated with SLM A and later only measuring the Gaussian component of the result via a SMF, we experimentally realize eq. 2.10 and can thus use SLM B to filter out LG mode components from the light state between the two SLM's.

3.2.1 Experimental Setup

In the experiment we use the Santec SLM-100 as the second SLM and replace the camera from fig. 3.4 with the SLM in the focal plane of the second lens in the 4f system. In order to be able to image

[3] while also considering the extent of the phase mask

the Fourier transform of the diffracted field from SLM B, we place a 500 mm lens at focal length away from the SLM and the camera. It is furthermore necessary to add an additional half waveplate between the two SLM's such that it is again ensured that the axis of polarization of the incoming beam at the second SLM matches its LCOS axis. The setup is pictured in fig. 3.6.

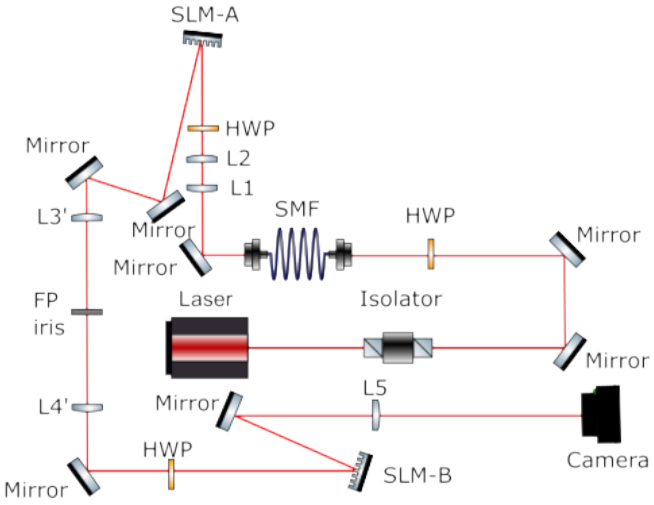

Figure 3.6: 2 SLM setup for mode projection with camera

3.2.2 Projective Measurements with a two SLM System

After an incoming beam of the electric field u has acquired the hologram phase profile from the first SLM and assumes the mode $u_A = \mathrm{LG}_{p\ell}$, a second SLM can be used to project a different mode $\mathrm{LG}_{p'\ell'}$ onto u_A by displaying a hologram calculated for the output field [4]

$$u_B = \mathrm{LG}^*_{p'\ell'} \tag{3.6}$$

The phase masks for both SLM's can then be calculated by substituting $u_A = \mathrm{LG}_{p\ell}$ for the first SLM and eq. 3.6 for the second SLM into eq. 2.18. Before incorporating the SMF into the experiment, we visually test this mode projection by imaging with a beam profiler. As is also the case for the following sections, we show only the $p = 1$ system with $\ell \in \{0, 1, 2, 3\}$ here, however in the appendix we also include the $p = 0$ and $p = 2$ systems in fig. A.2 and A.3. Fig. 3.7 shows an array of the resulting images as we capture each possible phase mask combination between the two SLM's.

In the resulting images it is qualitatively apparent that only the images on the top-bottom left-right diagonal (where $u_A = u_B^*$) contain a Gaussian component in their center. This can be explained by eq. 2.21, where only a mode projection that is the complex conjugate of a given mode will annul the imprinted pattern from the first SLM and revert the beam back to its original Gaussian form. We

[4] An important experimental consideration is the number of mirrors between the two SLM's. As each mirror conjugates the resulting field from the first SLM, in the case of an odd number of mirrors, the electric field before the second SLM is conjugated from the field at the first SLM. In such a case, it is necessary to further conjugate the phase mask of one of the SLM's.

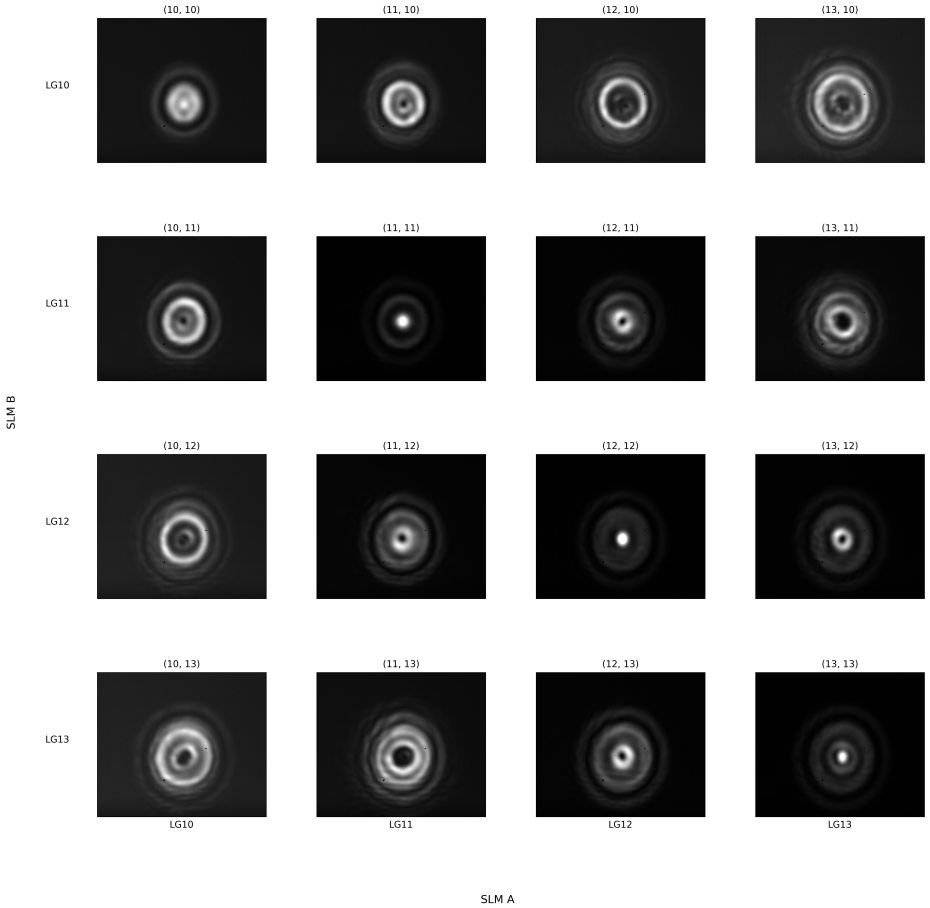

Figure 3.7: Mode projections for $p = 1, l \in \{0, 1, 2, 3\}$ captured with beam profiler

also notice a light ring around the the Gaussian component of the diagonal entries. This is a small non-Gaussian component which exists due to experimental inaccuracies.

CHAPTER 4

Reconstruction of LG Light States Using a 2 SLM Apparatus

Now that the experimental considerations have been handled and a sort of proof-of-concept measurement of the projective measurements has confirmed the efficacy of our setup, we are now able to implement a single mode fiber into the setup to filter out only the Gaussian component of the result of the projection. In sec. 4.1 we use this to essentially repeat the previous mode projection measurements. Using this information, we reconstruct a weighted and phase-delayed superposition of LG modes based on its constituent modes. In sec. 4.2 we address the optimization methods we test before our final measurements, and discuss what they reveal about some of the shortcomings of the experiment.

4.1 Reconstructing LG Light States

By measuring the percent fiber coupling of the mode projections into the single mode fiber, we can construct mode coincidence matrices that effectively show us the overlap between different modes (due to the orthonormality of the LG it is self-explanatory what we can expect). Furthermore, by measuring these matrices, we will see that this gives us sufficient information to be able to reconstruct simple LG mode superpositions by projecting various modes, measuring the coincidences, and comparing with the results from the mode coincidence matrices.

4.1.1 Measuring the Mode Coincidences Matrices

We now replace the final lens and camera from fig. 3.6 with a fiber coupling lens and SMF. We measure the power after the SMF with a photo diode. Since only the Gaussian component of the beam can couple into the fiber, the proportion of incoming power that is coupled into the SLM and then measured by the powermeter describes the share of the Gaussian mode in the overall light state.[1]

In fig. 4.1(a) and 4.1(b) we now essentially repeat the measurements from fig. 3.7 on this setup. The image on the left is the baseline measurement before the optimizations of sec. 4.2, and the image on the right is the final measurement taken after the implementation of these optimization methods.

[1] Since we are only interested in the intensity of the Gaussian component of the beam at this point, neither the Fourier-transforming property of the fiber coupling lens nor any phase factors hold any relevance.

The same is true for fig. A.4(a) and A.4(b) for $p = 0$ and fig. A.5(a) and A.5(b) for $p = 2$. We use a waist of $w_0 = 80$ SLM A pixels for each phase mask. On the z-axis of each plot we plot the coupling of the projective measurement into the SMF, or the proportion of power before the SMF that is coupled into the SMF and measured with the photo diode. Such a measurement is equivalent to the absolute square of the projective measurement of $\langle p', \ell'|$ onto $|p, \ell\rangle$

$$|\langle p', \ell'|p, \ell\rangle|^2 \tag{4.1}$$

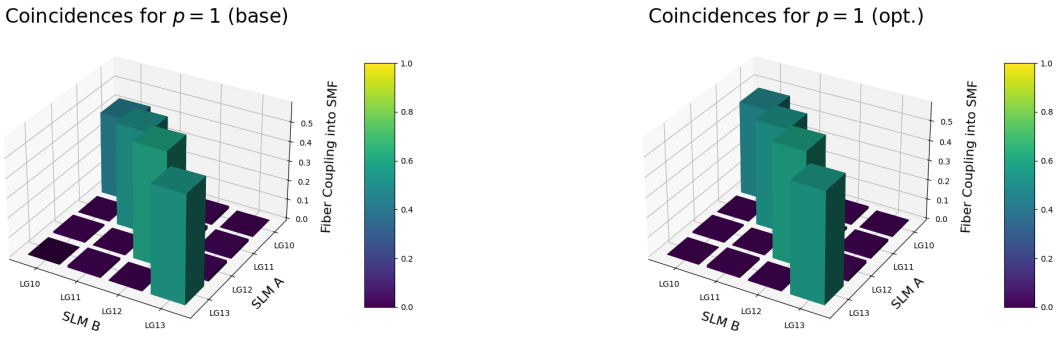

(a) Baseline coincidence measurements $p = 1$

(b) Optimized coincidence measurements $p = 1$

Figure 4.1: Mode projections in SMF for $p = 1, l \in \{0, 1, 2, 3\}$

In the optimized measurements we see a roughly $50 - 60\%$ fiber coupling along the diagonal matrix entries, with the off-diagonal elements being nonzero, but extremely small in comparison! The powermeter used[2] has an error of 3% [23]. We assume this is the only error source in the following calculations, although experimental inaccuracies such as optical alignment imperfections are also present. We also measure the first order diffraction efficiencies of each SLM $\eta_{A/B}$ to be

$$\eta_A = (29.43 \pm 0.01)\% \tag{4.2}$$
$$\eta_B = (14.17 \pm 0.01)\% \tag{4.3}$$

4.1.2 Decomposing Superimposed LG Mode States

In order to understand the process of decomposing an LG mode superposition into its constituent modes, we first start with an arbitrary state of superimposed LG modes which we experimentally generate on SLM A

$$u = \frac{1}{N} \sum_{p,\ell} \alpha_{p,\ell} |p, \ell\rangle \tag{4.4}$$

We then project a mode $\langle p', \ell'|$ onto u using SLM B and measure its coupling into the SMF

[2] Thorlabs Model PM100D

$$|\langle p', \ell'|u\rangle|^2 = \left|\langle p', \ell'|\frac{1}{N}\sum_{p,\ell}\alpha_{p,\ell}|p,\ \ell\rangle\right|^2 \tag{4.5}$$

$$= \left|\frac{1}{N}\alpha_{p',\ell'}\langle p',\ \ell'|p',\ \ell'\rangle\right|^2 \tag{4.6}$$

In the second step we use the orthonormality of the set of LG modes, as is also experimentally apparent for non-diagonal coincidence matrix elements in fig. 4.1(b). Since we already know $|\langle p',\ \ell'|p',\ \ell'\rangle|^2$ for all $p' \in \{0, 1, 2\}$ and $\ell' \in \{0, 1, 2, 3\}$ from the coincidence matrix of fig. 4.1(b) [3], we possess all the necessary information to solve for $|\alpha_{p',\ell'}|^2$

$$|\alpha_{p',\ell'}|^2 = |N|^2\frac{|\langle p', \ell'|u\rangle|^2}{|\langle p',\ \ell'|p',\ \ell'\rangle|^2} \tag{4.7}$$

$$= \beta^2_{p',\ell'} \tag{4.8}$$

In theory, by repeating these projective measurements for all $\langle p',\ \ell'| \in \{\langle p,\ \ell|\}$, eq. 2.12 would eventually be fullfilled, and one would be left with the complete set of the weighting factors, $\{\beta_{p,\ell}\}$, with all information about the intermodal phase differences of the state $\gamma_{p,\ell}$ being lost. In order to measure these phase differences, a quantum state tomography would be necessary, see [6–9]. In testing this, we find that due to experimental inaccuracies of the setup, only simple LG mode superpositions can be accurately decomposed and reconstructed on the current setup, and further optimizations will be necessary to analyze more complex superpositions.

We now analyze three different mode superpositions in eq. 4.9–4.11 by measuring the projections of $\langle 0,\ \ell|, \ell \in \{0, 1, 2, 3\}$ onto them

$$1.\ u = \frac{1}{\sqrt{2}}\left(|0,\ 3\rangle + |0,\ 1\rangle\right) \tag{4.9}$$

$$2.\ u = \frac{1}{\sqrt{2}}\left(|0,\ 3\rangle + e^{-i\frac{\pi}{2}}|0,\ 1\rangle\right) \tag{4.10}$$

$$3.\ u = \frac{2}{\sqrt{5}}\left(|0,\ 3\rangle + \frac{1}{2}|0,\ 1\rangle\right) \tag{4.11}$$

The projective measurements $|\langle p, \ell|u\rangle|^2$ are now substituted into eq. 4.8. We summarize the results in tab. 4.1.

We see the calculated β values are accurate to about 10% of the theoretical value, with the least accurate β factor being the weighted term of superposition 3. at around 20%. Nevertheless, the calculated β factors are sufficient enough to reconstruct the state without unreasonable error! We also see in the final column that eq. 2.12 is well fulfilled, and that the projected modes are essentially the only ones present in the superposition, thus excluding the possibility of any higher orders significantly

[3] We can use eq. 2.10 to eliminate the off-diagonal entries of the coincidence matrix, as their absolute square is several orders of magnitude smaller than that of the diagonals, however it does not suffice to assume the absolute square of the inner product of the diagonal entries is unity, as is visible in the coincidence matrix measurements.

Superposition	β_{00}	β_{01}	β_{02}	β_{03}	$\frac{\Sigma\beta^2}{N^2}$
1.	0.127 ± 0.004	1.104 ± 0.033	0.136 ± 0.004	0.919 ± 0.028	1.049 ± 0.044
2.	0.142 ± 0.004	0.942 ± 0.028	0.148 ± 0.004	1.072 ± 0.032	1.039 ± 0.044
3.	0.071 ± 0.002	0.609 ± 0.018	0.111 ± 0.003	0.949 ± 0.028	1.032 ± 0.047

Table 4.1: $\beta_{p,\ell}$ of state reconstruction measurement

affecting the results. We also notice an underestimation of the errors, as the only quantifiable error used in the error propagation is that of the powermeter, although in fact the optical impurities likely play a far greater role. This is also apparent in the slight deviation between superpositions 1. and 2., as any difference suggests the presence of rotational asymmetries in the optical elements of the setup.

4.2 Optimization Considerations

In this section we discuss some optimization methods that were tested with the goal of:

1. universally improving the fiber coupling of the diagonal matrix elements of the coincidence matrix;
2. minimizing discrepancies in the diagonal matrix elements such that they are all approximately equal.

For the optimization we only consider diagonal matrix elements, and analyze only $p = 1$ as it is the smallest nonzero radial mode. Fig. 4.2 contains the results of each method; we ultimately only incorporate the SLM B calibration of sec 4.2.3 for the final optimized measurements, since it is the only method that fullfills both of the above criteria. However, almost all the optimization methods lead to some relative improvement, and we discuss them regardless in the following sections.

4.2.1 Adjusting Beam Waist

All SLMs have a slight inherent curvature on their screen that distorts the output field. This is a major fault that must be characterized and compensated for in any (precise) SLM application. Unfortunately, this is quite difficult to measure and more worthy of a master's student project (s. outlook 5). Within the frame of this thesis, we circumvent this problem by using smaller-radius beams, such that the screen of the SLM locally approximates a plane where it interacts with the light [4]. This has the inverse effect that the resolution of the phase mask on the SLM is worsened. Thus, an optimum waist size for the phase masks must be found such that the combined effects of each problem are minimized.

We see in fig. 4.2 that decreasing the waist of the phase mask universally decreases the SMF coupling, whereas increasing it actually improves the coupling disproportionally for higher topological charges. For this reason we did not change the waist of our phase masks from $w_0 = 80$ for our final measurements. More than anything, these results suggest that more investigation in optimizing the beam waist is necessary.

[4] The wavefront curvature of the incoming light can also be characterized and compensated for with the SLM

Figure 4.2: Tested optimization methods and results for $p = 1$

4.2.2 Compensating for the Gaussian Intensity Profile of the Incoming Beam

When one calculates the hologram of the first SLM, one implicitly assumes a homogenous incoming beam at its screen, which in the experiment is in fact Gaussian. While this problem is also partially mitigated by using a small hologram waist compared to the actual beam radius, it is nevertheless worth addressing, especially since future projects may look to diffract larger portions of the beam, where this becomes more relevant. As was previously characterized by Kimberly[14], the waist of the laser beam is approximately 3.5 mm at the first SLM, or approximately 280 SLM A pixels. To compensate for the incoming Gaussian profile of the beam, in addition to projecting the desired output mode onto the beam, we also negate the incoming Gaussian component by calculating a phase mask for the output field

$$E_A = \mathrm{LG}_{00}^{*}(w_0 = 280)\mathrm{LG}_{p\ell}(w_0 = 80) \tag{4.12}$$

As one can see in fig. 4.2, compensating for this only improves the overall results slightly, and also disproportionally benefits higher topological charges. For these two reasons, we did not implement it in the final optimized measurements, however, especially if one is to diffract larger portions of the incoming beam with the hologram, where the Gaussian beam is less locally homogenous, this method could in principle be quite useful.

4.2.3 Calibrating the Grayscale Values of the 2nd SLM

Kimberly previously performed this calibration on the Hamamatsu SLM. Her results showed that when using the look-up table (LUT) provided by the manufacture, the SLM isomorphly mapped the grayscale values g /bit to the phase values φ, with $\varphi(g = 0) = 0$ and $\varphi(g = 255) = 2\pi$, and that no

further calibration steps were necessary beyond using this setting [14] p. 21. We now repeat this measurement on the setup of fig. 4.3 for SLM B.

In contrast to the rest of this thesis, we now turn the HWP before SLM B 22.5° from the the LCOS axis. In this way, the incoming field at the screen of the SLM has two equal components, one parallel and one perpendicular to the LCOS axis, such that only the parallel component experiences a phase retardation. On the screen of the SLM we display a phase mask in which every pixel has a uniform grayscale value. In the zeroeth order of diffraction this results in the field component parallel to the LCOS axis having an additional phase retardance corresponding to the grayscale value of the SLM, and the perpendicular component being otherwise reflected normally. This creates a state of elliptically-polarized light after the first SLM. By placing another HWP also at 22.5° after the SLM, we convert the elliptically-polarized light back to linearly-polarized light, however its angle of polarization now depends on the phase retardance of the LCOS-parallel component of light after the SLM. We now place a polarizing beam splitter (PBS) after the HWP, which allows transmission for only the horizontal component of the linearly polarized light, in order to measure this angle of polarization by measuring the transmitted power. Graphing this intensity against the grayscale value displayed on the SLM allows us to investigate the relation between grayscale value displayed on the SLM and the actual phase retardance experienced by the outgoing light.

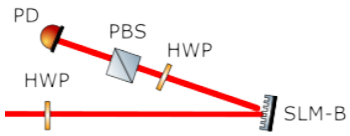

Figure 4.3: Setup for SLM B calibration

In the case of the Santec SLM, it is apparent from the calibration curve measurement in fig 4.4 that it contains a "dark" phase shift, thus making $\varphi(g = 0) > 0$. Additionally, the phase oscillation period is smaller than the total bit count 1023, thus making the bit-to-phase mapping no longer injective. This not only makes the calibration more necessary than previously, but it also thoroughly complicates it.

We fit[5] the measurements with eq. 4.13, where $I_{\max} \in [0, 1]$ is the maximum normalized intensity, Γ is the functional period in radians, ϕ_0 is the phase shift in radians, I_0 is the ambient power offset, and $\varphi(g)$ is the phase retardation of the SLM. The results of the fit are summarized in tab. 4.2.

$$I(g) = I_{\max} \cos^2\left(\Gamma g + \phi_0\right) + I_0 \quad \text{with} \quad \varphi(g) = 2(\Gamma g + \phi_0) \tag{4.13}$$

Substituting Γ and ϕ_0 into φ in eq. 4.13, we calculate the the corresponding g-values such that $\varphi = 0$ and $\varphi = 2\pi$.

$$g = -152 \longrightarrow \varphi = 0 \tag{4.14}$$

$$g = 595 \longrightarrow \varphi = 2\pi \tag{4.15}$$

This means the grayscale period of the SLM is 747 bit, and due to the dark phase shift of 152 bit, the phase retardation actually reaches 2π at $g = 595$.

[5] For the derivation of this model function, see Kurzbach p. 16–19 [14]

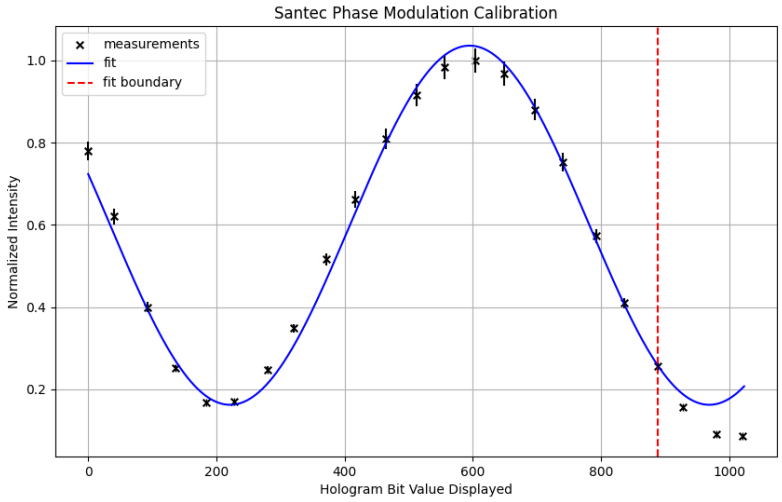

Figure 4.4: Calibration curve for the Santec SLM-100 used in the experiment

Parameter	Value
$I_{\max}$	0.874 ± 0.027
Γ	$(4.20 \pm 0.05)10^{-3}$ rad
ϕ_0	(0.641 ± 0.026) rad
I_0	0.162 ± 0.015

Table 4.2: SLM B Calibration Fit Parameters

In order to achieve an isomorph map between $\varphi(g'') : [0, 747] \twoheadrightarrow [0, 2\pi]$ with a transformed coordinate system g'', we must address both the dark phase shift and incorrect period. To first address the period, we perform an initial coordinate transformation $[0, 1023] \twoheadrightarrow [0, 747]$, $g \mapsto g'$ that rescales the period.

$$g' = \frac{747}{1023} \cdot g \tag{4.16}$$

We can then account for the dark phase shift by transforming $g' \mapsto g''$ with

$$g'' = \begin{cases} g' - 152 & : g \geq 152 \\ 747 - g' & : g < 152 \end{cases} \tag{4.17}$$

Heuristically, this is equivalent to copying the grayscale values below the dark shift 152 and pasting them one period forward, left of the 2π shift. It is then clear for $\varphi(g'')$ that $\varphi(g'' = 0) = 0$ and $\varphi(g'' = 747) = 2\pi$ [6]. A visual comparison of an uncalibrated (left) and calibrated (right) LG_{12} SLM

[6] It was later discovered that, in theory, only the first coordinate transformation $g \mapsto g'$ is necessary to properly calibrate the grayscale values. Since only the relative phase is relevant for the light modulation, adding a constant phase shift in $g' \mapsto g''$ should have no effect outside of shifting the calibration measurement of fig. 4.4, and the improvement in the

B phase mask are shown in fig. 4.5.

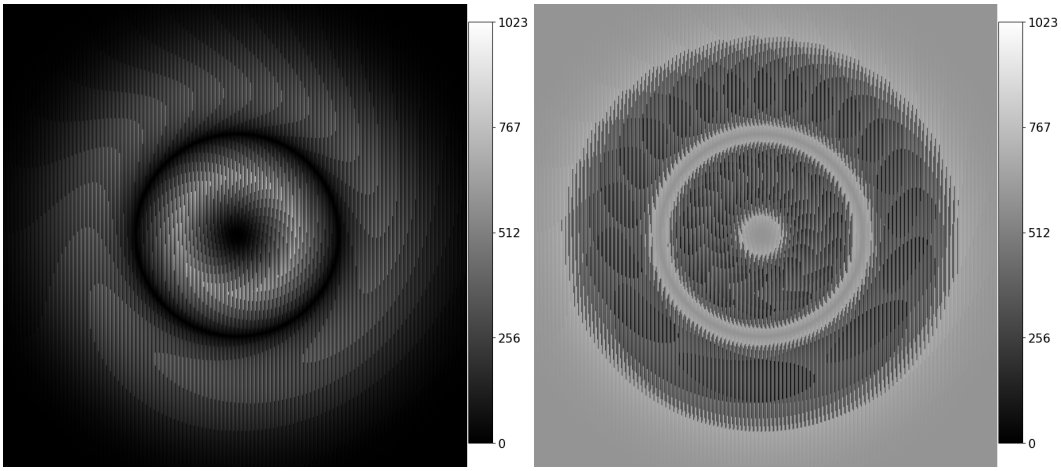

Figure 4.5: Uncalibrated (left) and calibrated (right) LG_{12} phase mask for SLM B

By performing this coordinate transformation, we see in fig. 4.2 that the coupling of all the diagonal matrix elements are improved, especially $(10, 10)$ which has relatively less coupling to the other modes in the baseline measurement. This method was the only one used in the final coincidence measurements, and universally improved the couplings. As such, it should be used in all future use of the second SLM.

4.2.4 Accounting for the Varying Outer Ring Radii of LG Modes

A hypothesis that we had while optimizing was that the disparities in the diagonal matrix elements might be a result of the outer radii of higher-order modes experiencing different optical nonuniformities than the lower order modes. We thus investigate what happens if the radii of the intensity maximums of the outermost ring of each mode are artificially scaled down to match the radius of the LG_{00} mode. This is accomplishable by scaling down the waist for the calculation of the phase mask by the factors in fig. 4.6. We hereby assume that the beam radius is approximately equal to the beam waist, as our propagation distance is far below the Rayleigh length. We accordingly lose a great deal of resolution for higher-order modes at each SLM, while lower-order modes remain relatively constant.

What one can observe is that, while the couplings become worse for all $\ell > 0$ modes, they also become more uniform as it disproportionally affects higher topological charges. For certain applications, this could be quite useful, although strictly speaking one loses orthonormality of the modes by taking LG modes from different waist sets. It also suggests the reason for $\ell = 0$ modes' generally lower coupling is a relatively lower SLM resolution, since they are spatially smaller than the other modes.

results in fact stems from the rescaling of the period.

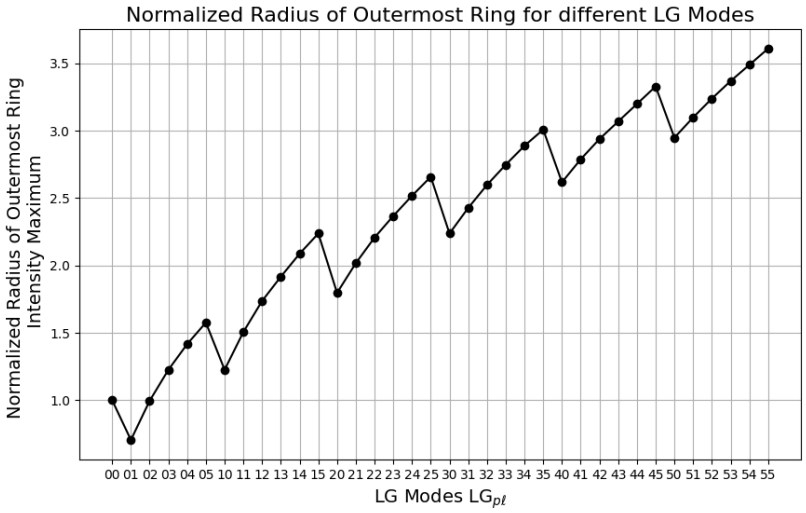

Figure 4.6: Outer radius normalization of LG_{00}–LG_{55}

CHAPTER 5

Summary and Outlook

In the first chapter we addressed the fundamental theory of this thesis: the definition and properties of LG modes, the creation of proper CGH's for their generation, and the Fourier optics principles which dictate our experimental considerations and simulations. Unfortunately, although these fundamental topics have already been extensively covered in the theses of the previous bachelor students of this project, as a standalone document my thesis must re-address them for completeness. In this spirit, I attempt to avoid repetition wherever possible in my descriptions of them, and, when unavoidable, to present things in a novel way more relevant to my thesis.

In the second chapter we make the transition from the previous Bachelor's thesis to the final setup of mine. We start with the single SLM setup and the telephoto lens to image the pure LG modes, and analytically check the quality of the generated LG_{00}–LG_{33} modes. After analytically confirming a high mode purity, we expand the setup to a 4f system to eliminate the additional phase term of eq. 2.27 and map the field at the screen of the first SLM to that of the second. Using this setup, we capture the first superpositions of LG modes. Next, we implement the second SLM into the 4f system and present the process of utilizing it to perform a mode projection. This is tested by imaging the resulting intensity patterns with a beam profiler, in which one can qualitatively observe a Gaussian component in only the diagonal photos, where the original mode was correctly converted back to Gaussian (all other entries contain no discernible Gaussian component).

In the final chapter, we introduce the SMF to filter out the non-Gaussian components from the projective measurements. We are thus able to measure the coincidence matrices between the displayed modes on both SLM's, and observed near-zero coupling into the SMF for the off-diagonal matrix elements, and $> 50\%$ fiber coupling for the diagonal elements, thus experimentally realize eq. 2.10. With the information of the individual couplings, we are able to decompose a superposition of LG modes into its constituent mode components by measuring the couplings into the SMF. We are thus able to reconstruct simple superpositions with about 10% accuracy, and show that by measuring only topological charges $\ell \leq 3$ for $p = 0$, we can already fulfill the completeness of the set of LG modes in eq. 2.12 to a high accuracy. We also analyze some optimization methods to improve the and standardize the couplings of the diagonal matrix elements. Ultimately, only a calibration of SLM B which is performed in this section was implemented for the final measurements, however, the other optimization methods hold some experimental relevance, as they help illuminate shortcomings in the current experimental setup. The LG_{00} compensation does in fact improve the couplings for higher topological charges; we didn't implement it in the end solely because it increases the inequality of the

couplings between lower and higher modes. For future experiments with higher beam radii, where the incoming Gaussian beam is less approximately homogenous at the screen of the first SLM, this optimization method could actually be worth incorporating. Furthermore, we see how the mode outer radius compensation greatly improves the uniformity of the diagonal components, as it eliminates the additional error sources that the higher-radii modes would experience, such as SLM screen curvature. However, it also reduces the resolution of the SLM for these modes, which in the end lowers the couplings of the higher order modes to the level of LG_{00}, which is why we ultimately do not incorporate it. Lastly, using a smaller waist leads to universally worsened couplings, while a larger waist leads to improved couplings, but disproportionally for LG_{11} –LG_{12}. This would for instance suggest that the effect of SLM screen curvature may not negatively affect the results as much as reducing the resolution of the SLM's, and that a waist size optimization of each SLM is absolutely necessary as a further optimization step. While in this thesis the power efficiency of the setup is hardly a consideration, for future single photon experiments it will be. The same spatial grating period from SLM A was used for SLM B, however the first order diffraction efficiency of SLM B is about half that of SLM A, and the reason for which is unclear; for both SLM's this will have to be characterized and optimized as well. This underlines a general need for power and hologram waist efficiency characterization and optimization for both SLM's.

Going forward, there still remain some operational and optimizational considerations before the dual SLM system can be implemented into the main experiment. The first and perhaps most necessary optimization is a curved wavefront and SLM screen curvature characterization and compensation, as was once completed in the Meschede Group (Zhou-Hanf sec. 4.3 [24]), along with a characterization of other inherent SLM inaccuracies such as pixel cross-talk. One could apply the Gerchberg-Saxton algorithm to iteratively correct these errors. Of course there also exist optical and alignment imperfections in the setup that could be improved to optimize results.

Furthermore, while we were able to easily calculate the coupling into the SMF by measuring the incoupling and outcoupled power before and after the SMF, in the main experiment only the outcoupled power will be measured. In fig. A.6 we measure the incoupling power before the SMF for various LG modes displayed on SLM B (with only a grating displayed on SLM A). As one can see, their measured power varies greatly, in contradiction with the othernormality of the set of LG modes. Of course, by extension this makes the outcoupled power of varying modes highly variable in some cases. This nonuniformity likely depends on multiple factors, such as varying diffraction efficiencies between modes for each respective SLM, optical errors, and inherent SLM errors disproportionally affecting certain modes. The effect in the end is that, although most modes for a certain p regime have around the same coupling, the power measured after the SMF can vary as much as 300% between different topological charges. This must be optimized so that certain modes are not suppressed in comparison to others. We didn't test the effect of the optimization methods of chap. 4 on this issue, however they could possibly help. Of course there also still remains the task of maximizing the couplings of the diagonal entries, improving their uniformity, and minimizing the couplings of the off-diagonal entries of the coincidence matrices, however improvements here will likely come as a natural consequence of the aforementioned optimization steps.

APPENDIX A

Appendix

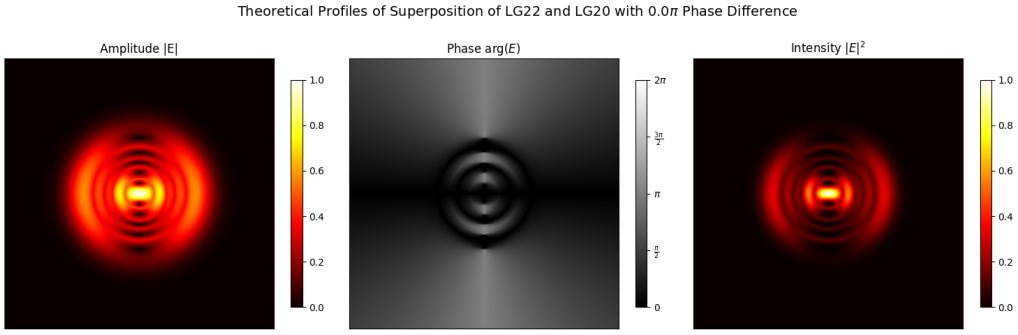

(a) No phase difference no weighting

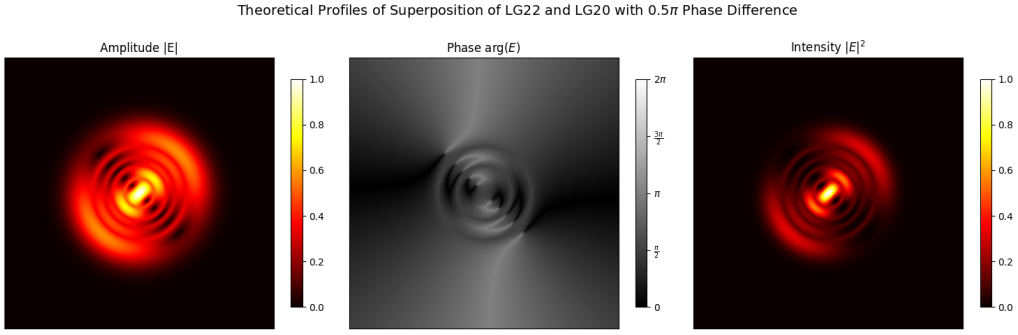

(b) LG_{20} with $\frac{\pi}{2}$ phase difference

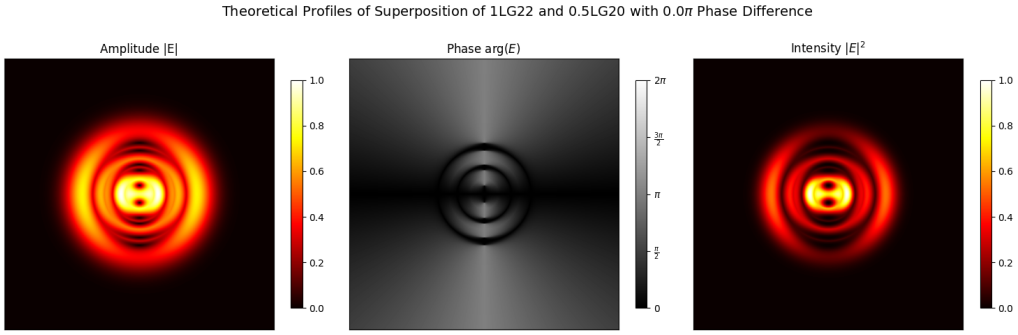

(c) LG_{20} with $\frac{1}{2}$ weighting

Figure A.1: Mathematical amplitude, phase, and intensity of: (a) $LG_{20} + LG_{20}$; (b)$LG_{20} + e^{-i\frac{\pi}{2}} LG_{20}$; and (c) $LG_{20} + \frac{1}{2}LG_{20}$

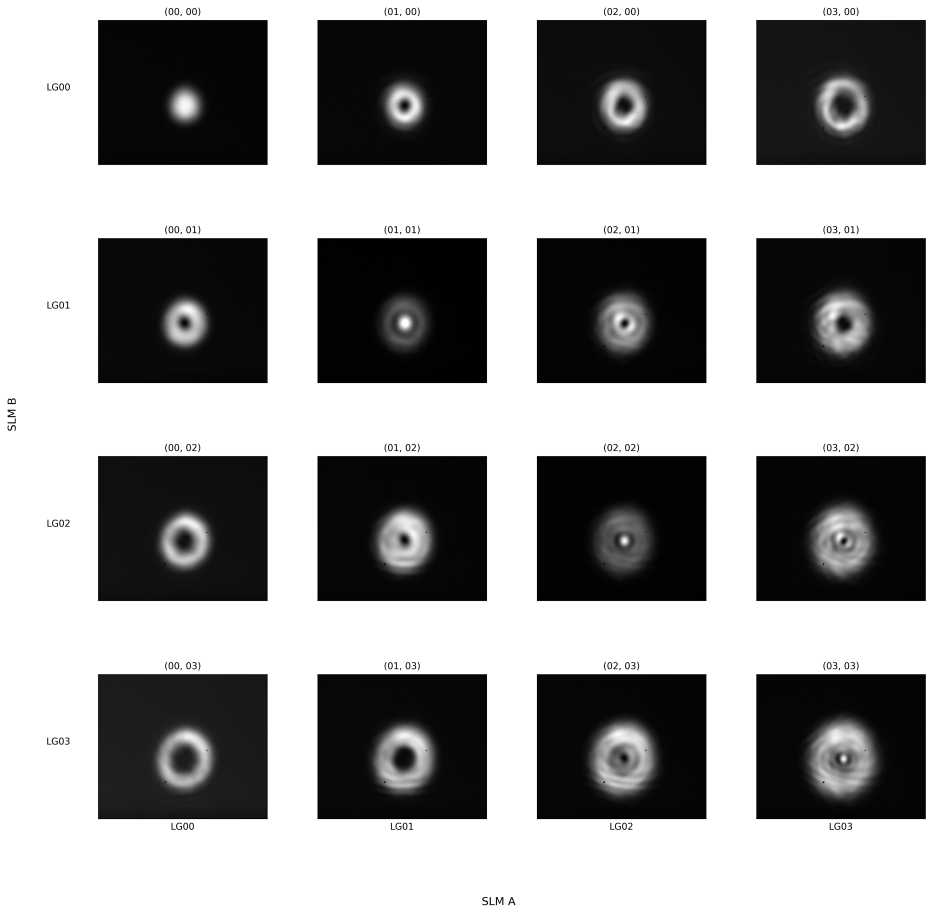

Figure A.2: Mode projections for $p = 0$, $\ell \in \{0, 1, 2, 3\}$ captured with beam profiler

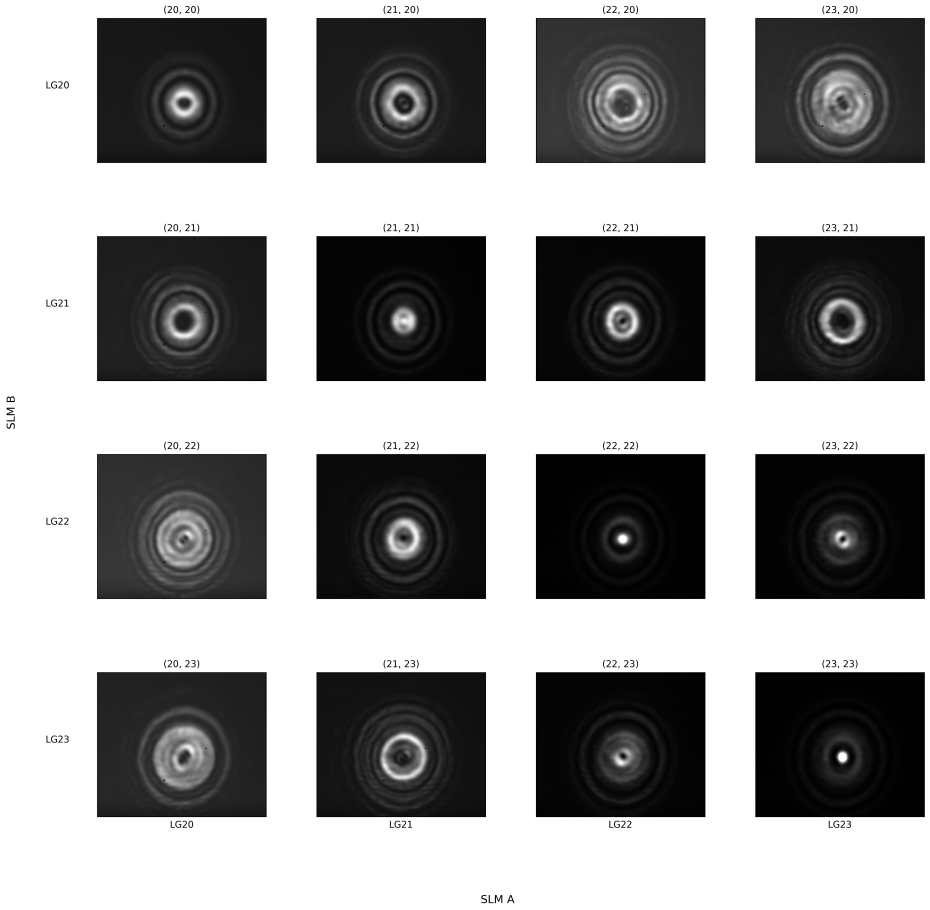

Figure A.3: Mode projections for $p = 2$, $\ell \in \{0, 1, 2, 3\}$ captured with beam profiler

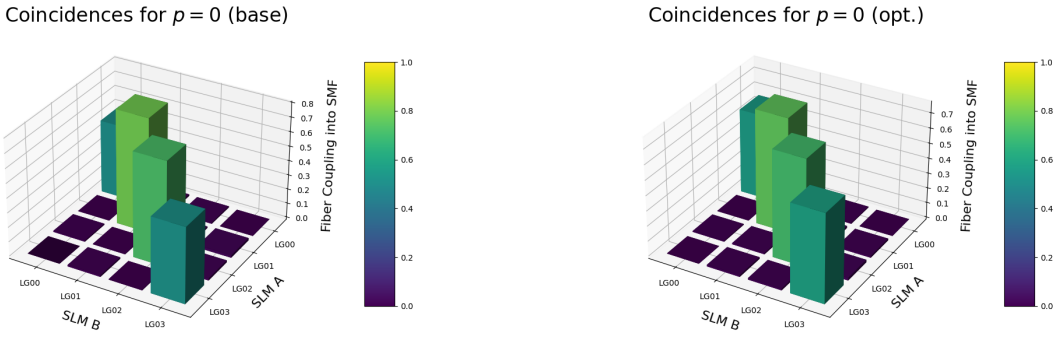

(a) Baseline coincidence measurements $p = 0$

(b) Optimized coincidence measurements $p = 0$

Figure A.4: Mode projections in SMF for $p = 0$, $\ell \in \{0, 1, 2, 3\}$

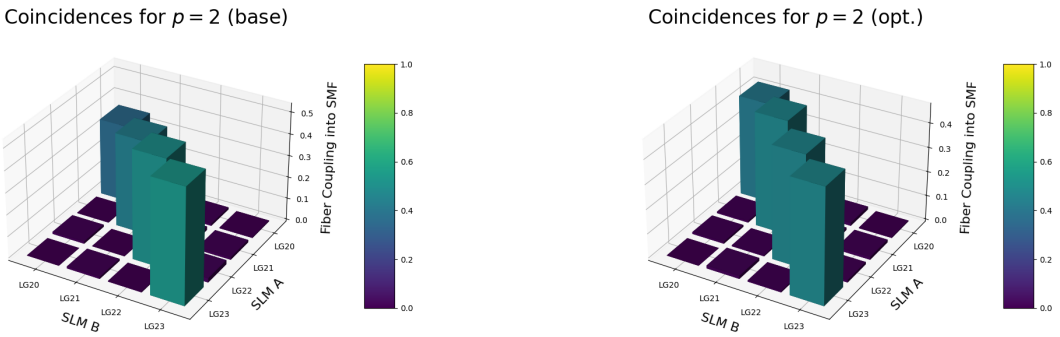

(a) Baseline coincidence measurements $p = 2$

(b) Optimized coincidence measurements $p = 2$

Figure A.5: Mode projections in SMF for $p = 2$, $\ell \in \{0, 1, 2, 3\}$

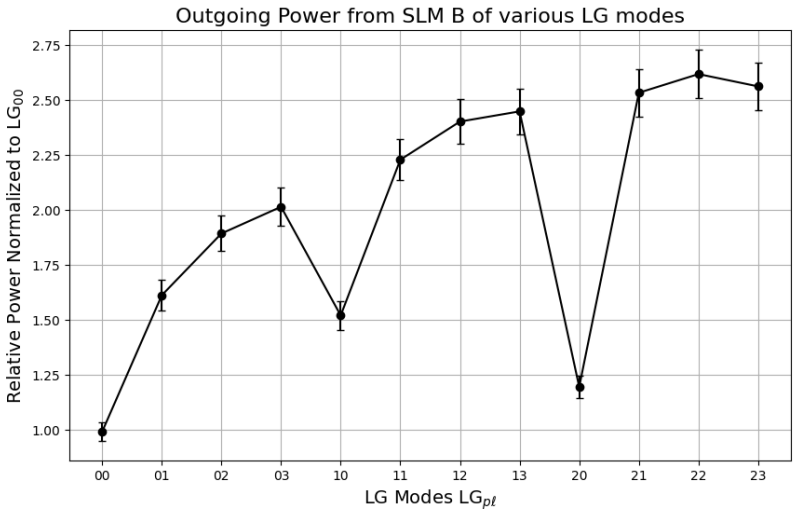

Figure A.6: Power output of various LG modes from SLM B

Bibliography

[1] A. Forbes, A. Dudley and M. McLaren,
Creation and detection of optical modes with spatial light modulators,
Adv. Opt. Photon. **8** (2016) 200,
URL: https://opg.optica.org/aop/abstract.cfm?URI=aop-8-2-200 (cit. on p. 1).

[2] F. Bouchard et al., *Measuring azimuthal and radial modes of photons*,
Opt. Express **26** (2018) 31925,
URL: https://opg.optica.org/oe/abstract.cfm?URI=oe-26-24-31925
(cit. on p. 1).

[3] H. Qassim et al., *Limitations to the determination of a Laguerre-Gauss spectrum via projective, phase-flattening measurement*, J. Opt. Soc. Am. B **31** (2014) A20,
URL: https://opg.optica.org/josab/abstract.cfm?URI=josab-31-6-A20
(cit. on pp. 1, 4).

[4] L. Zhu and J. Wang, *Arbitrary manipulation of spatial amplitude and phase using phase-only spatial light modulators*, Scientific reports **4** (2014) 7441 (cit. on pp. 1, 14).

[5] N. Matsumoto et al., *Generation of high-quality higher-order Laguerre-Gaussian beams using liquid-crystal-on-silicon spatial light modulators*, J. Opt. Soc. Am. A **25** (2008) 1642,
URL: https://opg.optica.org/josaa/abstract.cfm?URI=josaa-25-7-1642
(cit. on pp. 1, 6, 14).

[6] E. Bolduc, N. Bent, E. Santamato, E. Karimi and R. W. Boyd, *Exact solution to simultaneous intensity and phase encryption with a single phase-only hologram*, Opt. Lett. **38** (2013) 3546,
URL: https://opg.optica.org/ol/abstract.cfm?URI=ol-38-18-3546
(cit. on pp. 1, 7, 11, 21).

[7] N. Bent et al., *Experimental Realization of Quantum Tomography of Photonic Qudits via Symmetric Informationally Complete Positive Operator-Valued Measures*,
Phys. Rev. X **5** (4 2015) 041006,
URL: https://link.aps.org/doi/10.1103/PhysRevX.5.041006 (cit. on pp. 1, 21).

[8] V. D'Ambrosio et al.,
Test of mutually unbiased bases for six-dimensional photonic quantum systems,
Scientific reports **3** (2013) 2726 (cit. on pp. 1, 21).

[9] B. Jack et al.,
Precise quantum tomography of photon pairs with entangled orbital angular momentum,
New Journal of Physics **11** (2009) 103024 (cit. on pp. 1, 21).

[10] E. Schonbrun et al., *3D interferometric optical tweezers using a single spatial light modulator*, Opt. Express **13** (2005) 3777, URL: https://opg.optica.org/oe/abstract.cfm?URI=oe-13-10-3777 (cit. on p. 1).

[11] D. Preece, *Novel uses of spatial light modulators in optical tweezers*, PhD Thesis: University of Glasgow, 2011, URL: https://theses.gla.ac.uk/2619/ (cit. on p. 1).

[12] L. W. Clark, N. Schine, C. Baum, N. Jia and J. Simon, *Observation of Laughlin states made of light*, Nature **582** (2020) 41, ISSN: 1476-4687, URL: http://dx.doi.org/10.1038/s41586-020-2318-5 (cit. on p. 1).

[13] O. Firstenberg, C. S. Adams and S. Hofferberth, *Nonlinear quantum optics mediated by Rydberg interactions*, Journal of Physics B: Atomic, Molecular and Optical Physics **49** (2016) 152003, ISSN: 1361-6455, URL: http://dx.doi.org/10.1088/0953-4075/49/15/152003 (cit. on p. 1).

[14] K. Kurzbach, *Generation and Detection of Optical Beams with Orbital Angular Momentum using a Spatial Light Modulator*, Bachelor's Thesis: Universität Bonn, 2024, URL: https://www.nqo.uni-bonn.de/publications/publications/2024-kimberly-kurzbach-bachelor.pdf (cit. on pp. 1, 11, 23, 24).

[15] C. Kunert, *Generation and Optimization of Laguerre-Gaussian Modes Using a Spatial Light Modulator: A Simulation Approach*, Bachelor's Thesis: Universität Bonn, 2024, URL: https://www.nqo.uni-bonn.de/publications/publications/2024-celina-kunert-bachelor.pdf (cit. on pp. 1, 8, 12).

[16] S. Linden, *Optik und Wellenmechanik*, Lecture Script for *physik311*, Available at: https://www.pi.uni-bonn.de/linden/en/media/optik.pdf, 2024 (cit. on p. 3).

[17] J. W. Goodman, "Introduction to Fourier optics", 1969, URL: https://api.semanticscholar.org/CorpusID:118908270 (cit. on pp. 3, 8, 9).

[18] *LCOS-SLM modules*, Hamamatsu Photonics K.K., 2015 (cit. on p. 6).

[19] *LCOS-SLM Operational Manual*, Version 3.1, Santec Corporation, 2018 (cit. on p. 6).

[20] J. A. de Haan, *Holographic Generation of Arbitrary Intensity Patterns*, Bachelor's Thesis: Universität Bonn, 2022, URL: https://www.nqo.uni-bonn.de/publications/publications/2022-jan-de-haan-bachelor.pdf (cit. on p. 8).

[21] *Technical description and instruction manual of an extended cavity diode laser ECDL-7830R (S/N 121111)*, Nonlinear Quantum Optics Group, URL: https://wiki.nqo.uni-bonn.de/images/ECDL-7830R_121111_Vitaly.pdf (cit. on p. 11).

[22] *LaserCam-HR II Data Sheet*, Coherent Laser Technologies, 2018 (cit. on p. 12).

[23] *Digital Handheld Optical Power and Energy Meter Console*, Thorlabs, Inc, 2015, URL: https://www.thorlabs.com/newgrouppage9.cfm?objectgroup_id=3341 (cit. on p. 20).

[24] W. Zhou-Hanf,
Robust Holographic Generation of Arbitrary Light Patterns: Method and Implementation,
Master's Thesis: Universität Bonn, 2018,
URL: https://quantum-technologies.iap.uni-bonn.de/de/diplom-theses.html
(cit. on p. 30).

List of Figures

List of Tables

Acknowledgements

I would like to thank Sebastian for giving me the opportunity to write my thesis in this group and for offering excellent guidance throughout.

I would also like to thank Prof. Wang for agreeing to be the second examiner of my thesis.

I would like to thank Wolfgang for always giving valuable insights and for his approachability.

I would like to thank Daniil for the many questions answered and problems solved as my advisor, and for his openness and friendliness that made me feel very comfortable in the group.

I would like to thank all of RQO (Nina, Lukas, and Simon) for the valuable time they took to help me with many different problems, and most importantly for creating an environment that made me feel very welcome and made the entire process very enjoyable.

I would like to thank Chris for his support and for being a great office and lab partner.

I would like to thank YQO for being very generous with lending me the beam profiler.

As a whole, I would like to thank the entire rest of the NQO group for making this a very enriching and enjoyable experience on both a personal and academic level.

Lastly, I would like to thank my family and my close friends GE, PAM, and MBB who've given me a lot of support during this thesis in countless ways.